Enhanced catalytic activity of nanoporous Au for the efficient electrochemical reduction of carbon dioxide

M. Nur Hossain, Zhonggang Liu, Jiali Wen, Aicheng Chen*

Electrochemical Technology Centre, Department of Chemistry, University of Guelph, 50 Stone Road East, Guelph, ON, N1G 2W1, Canada

A B S T R A C T

Herein, we demonstrate a three-dimensional (3D) nanoporous (NP) structure, resulting from electrochemical alloying/dealloying of polycrystalline Au in a mixture of ethylene glycol and 1.5 M $ZnCl_2$, for the efficient electrochemical reduction of CO_2 to CO. The formed NP Au-Zn was further thermally treated with H_2SO_4, whereupon a significant enhancement of its electrocatalytic activity was achieved. The resulted NP Au exhibited over 65 times higher current density compared to a polycrystalline Au surface, and three times higher current density than NP Au-Zn at −0.6 V vs. RHE in a CO_2-saturated 0.1 M $NaHCO_3$ solution. In addition, the Faradaic efficiency (FE) of the formed NP Au at the applied potentials of −0.6 V for 10 h was extremely high (95.9%), revealing that the surface structure played a critical role in the electrochemical reduction of CO_2. The superior catalytic activity, high production rate, excellent FE, and high stability make the unique NP Au developed in this study a promising electrocatalyst for the efficient and selective conversion of CO_2 to CO.

1. Introduction

Carbon dioxide (CO_2) plays a primary role in climate change, where the concentration of CO_2 in the atmosphere has been increasing rapidly since the Industrial Revolution, and has recently reached its highest level (~405 ppm). Since the average global temperature is rising, and the Earth's climate system is being altered as well, scientists are investing great efforts in the identification of strategies to minimize CO_2 emissions [1,2]. However, it would be very helpful, beyond thinking only of ways to reduce or stop CO_2 emissions into the environment, if CO_2 might be transformed into renewable fuels. Among various technologies to convert CO_2, the electrochemical method is considered a promising pathway to transform CO_2 into valuable chemicals and fuels. The primary target for the electrochemical technology is to develop an efficient electrocatalyst for robust reduction of CO_2 with high selectivity, low overpotential, fast kinetics, high stability and high energy efficiency.

CO_2 is recognized as an inert molecule, fully oxidized and thermodynamically stable, which represents significant challenges toward its chemical transformation to useful carbon based products [3–5]. It is therefore essential to develop an efficient technology that may convert CO_2 into valuable chemicals via a cost-effective process, while achieving high efficiency. It has been reported that the electrochemical reduction of CO_2 can produce hydrocarbons, aldehyde and alcohols [6–14]. Considerable efforts have been invested in deciphering the

fundamental kinetics of the electrochemical reduction of CO_2, both experimentally and theoretically [8–12]. Researchers have identified a wide variety of catalysts that have the ability to reduce CO_2 in aqueous electrolytes [9,13,14]. In particular, Au is known as a promising catalyst that exhibits high activity and selectivity to form CO from the electrochemical reduction of CO_2 [15]. CO constitutes an important industrial chemical that may be converted to various synfuels and valuable chemicals using the Fischer–Tropsch process [16,17]. Different classes of Au electrodes have been reported for the electrochemical reduction of CO_2, including nanoparticles [15], nanowires [18], nanoneedles [1], porous films [19,20], and gold-based nanomaterials [21], revealing that nanostructured Au electrodes can impart much higher catalytic activity compared to polycrystalline Au electrodes [22,23]. This may be attributed to large electrochemically active surface areas (EASAs) and different crystal facets [12,14,24]. Experimental results have also shown that the structures and morphologies of these nanocatalysts play a significant role in the enhancement of catalytic activity, for instance, lowering the overpotential, improving the Faradaic efficiency, and accelerating the reaction rate for the electrochemical reduction of CO_2 [8–12,25].

Recently, porous materials have gained great attention in the development of high-performance catalysts for the electrochemical reduction of CO_2 due to the improved catalytic activity and selectivity over their corresponding smooth surfaces [19,20]. Pang et al. synthesized porous Cu via simultaneous Cu electrodeposition and hydrogen

evolution followed by wet oxidation, and investigated the oxide-derived porous Cu for CO_2 reduction, showing high selectivity of the C_2H_4 production at a high pH of the electrolyte [26]. Nanoporous Ag, prepared by thermal alloying and two-step dealloying, was also tested for the CO_2 electrochemical reduction by Li et al., revealing ∼92% selectivity of CO production with a much higher current density than the polycrystalline Ag [13]. Moreover, a mesostructured porous Au was prepared via electrodeposition using a polystyrene template, showing that the diffusional gradient within the porous film could suppress the hydrogen evolution reaction, leading to high selectivity for CO production [20]. However, current CO_2 electroreduction technologies are still quite distant from industrial applicability, due to high overpotential and slow reduction rates. Therefore, further efforts are required to elucidate fundamental kinetics, and to tailor high-performance electrocatalysts for CO_2 conversion. In the present study, we have demonstrated a 3D novel NP Au, resulting from a facile electrochemical alloying/dealloying approach followed by acid treatment. It possessed an extensive EASA and new active sites, and exhibited excellent electrocatalytic activity, high selectivity, low overpotential, and fast kinetics for the efficient conversion of CO_2 to CO.

2. Experimental section

2.1. Chemicals and materials

Gold microwire (127 μm in diameter, 99.99%), $ZnCl_2$ (≥98.0%), H_2SO_4 (99.99%), and $NaHCO_3$ (≥99.0%) were obtained from Sigma Aldrich; Zn foil (99.98%, 0.25 mm thick) was purchased from Alfa Aesar; Ethylene glycol (Analytic grade) and ultrapure carbon dioxide (99.999%) were purchased from ACP Chemical Inc. and Praxair, respectively. All chemicals were used directly as received. All of the solutions were prepared using double-distilled water (purified by a Nanopure Diamond water purification system, 18.2 MΩ cm).

2.2. Fabrication of nanoporous Au electrodes

To prepare an Au microelectrode, a 10 cm long copper wire was passed into an 8.0 cm glass tube that had its end dipped into a conductive gold paste (Heraeus Inc., USA), which acted as conductive adhesive. Subsequently, a 5.0 or 8.0 mm long gold microwire was carefully passed through the glass tube until the microwire was gently attached to the copper wire. An epoxy resin was employed to wrap the top and end of the glass tube. The prepared electrode was subsequently introduced into an oven at 60 °C for 90 min, followed by being held vertically in ambient air to cool.

The NP Au-Zn was fabricated via an electrochemical alloying/dealloying method, which was based on a three-electrode system, where the Au microelectrode, Zn foil, and Zn wire served as the working electrode, counter electrode, and reference electrode, respectively. The alloying/dealloying of the Au microelectrode was carried out in a mixture of ethylene glycol and 1.5 M $ZnCl_2$ via cyclic voltammetry (CV) in the potential range between −0.80 and +1.80 V (vs. Zn) at a scan rate of 10 mV s^{-1} for different cycles at 110 °C. The fabricated NP Au-Zn was further treated using the procedure as follows: the NP Au was soaked in concentrated H_2SO_4 for 30 min, dried in an oven at 60 °C for 2 h, and calcinated at 150 °C in a furnace for 1 h. After cooling down, the electrode was thoroughly washed using pure water; and the obtained electrode was denoted as the NP Au.

2.3. Structural characterization

The surface morphology and EDX analysis of the prepared samples were investigated by a field emission scanning electron microscope (FE-SEM, Hitachi SU-70) at 20 kV. X-ray diffraction (XRD) patterns were collected using a Phillips PW 1050-3710 with Cu Kα1 of 1.5406 Å (radiation source) to determine the structural characteristic of the

prepared Au electrodes. Data was obtained in the range from 10° to 90° of 2θ with a step width of 0.01°/2θ. XRD data analysis was performed using X'Pert High Score Plus software. X-ray photoelectron spectroscopy (XPS) spectra were recorded via a Thermo Fisher XPS system, where the size of the X-ray spot was 400 mm, with an Al Kα monochromatic source. All of the XPS data was processed using XPSPEAK 4.1 software.

2.4. Determination of active sites

The surface active sites of the Au, NP Au-Zn and NP Au electrodes were characterized using lead underpotential deposition (Pb UPD) [20]. All the electrodes initially were cleaned in an Ar-saturated 0.1 M $KClO_4$ electrolyte by employing CV scanned between −0.8 and 1.35 V (vs. Ag/AgCl) at a scan rate of 50 mV s^{-1} for 20 cycles. The Pb UPD was performed by recording CVs in the range of −0.8 to 0.6 V vs. Ag/AgCl at a scan rate of 20 mV s^{-1} in an Ar-saturated 0.1 M $KClO_4$ solution containing 50 μM $Pb(NO_3)_2$.

2.5. Electrochemical characterization

A CHI660E electrochemical workstation (CH Instrument Inc. USA) was employed to carry out Linear Sweep Voltammetry (LSV) and chronoamperometry (CA) utilizing a three-electrode cell system. Electrochemical Impedance Spectroscopic (EIS) measurements were performed using a VoltaLab potentiostat (PGZ-301), where the frequency was varied from 100 kHz to 40 mHz with an A.C. voltage amplitude of 10 mV. Z-View software was used to fit the data and to obtain an equivalent circuit for the EIS experimental data. An Ag/AgCl (3.0 M KCl) and a platinum coil (10 cm^2) were used as the reference electrode and the counter electrode, respectively. The solution was initially purged with CO_2 for 20 min in order to achieve a CO_2-saturated condition, after which it was continuously purged into the solution while performing the analysis. All electrochemical experiments were conducted at ambient room temperature (20 ± 2 °C). All of the electrode potentials cited in the present work were converted to the reversible hydrogen electrode (RHE) reference scale using the following equation:

E(vs. RHE) = E (vs. Ag/AgCl) + 0.210 V + 0.0591 V × pH

The reaction kinetics of CO_2 reduction at the different Au electrodes was analyzed using the Tafel plot. The data was obtained from the LSV curves recorded at a scan rate of 2 mV s^{-1} in the CO_2-saturated 0.1 M $NaHCO_3$ electrolyte.

2.6. Electrochemically active surface area (EASA) measurement and roughness factor (RF) calculation

To clean the Au, NP Au-Zn and NP Au electrodes and to determine their EASAs, CV was continuously run between 0.0 and +1.5 V (vs. Ag/AgCl) in a 0.1 M H_2SO_4 solution at a scan rate of 20 mV s^{-1} until a stable CV curve was obtained. The formation of gold oxide in the forward scan, and subsequently, the reduction of the formed gold oxide in the reverse scan occurred, respectively. The EASA was determined by integrating the reduction peak (centered at ∼0.9 V vs. Ag/AgCl) to calculate the charge that was associated with the reduction peak. The ratio between the calculated EASA and the geometrical area of the electrode is known as the roughness factor, and may be calculated using the following formula:

RF = Electrochemical surface area/Geometrical area

2.7. Product analysis

A three-compartment electrochemical cell, where the working electrode compartment was gas-tight, and CO_2 was initially purged for
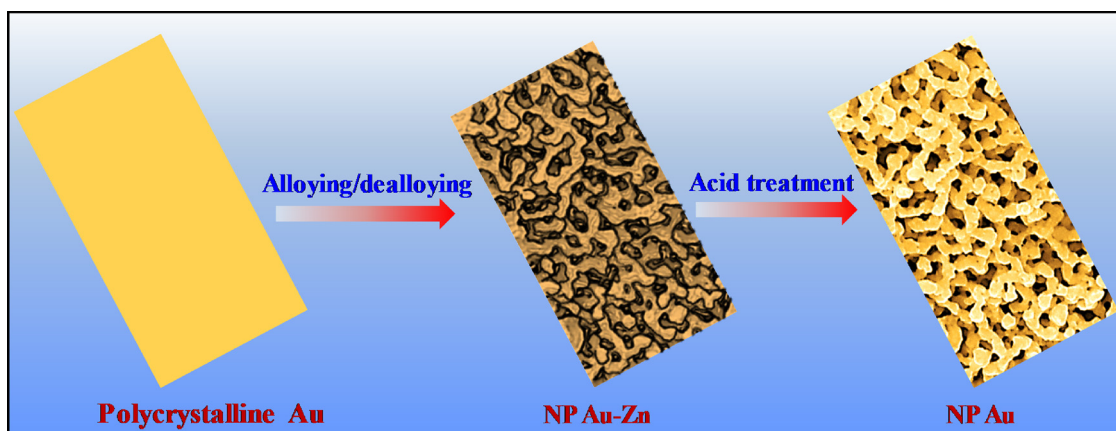
Scheme 1. Schematics of the preparation of the NP Au-Zn and the NP Au electrodes.

60 min. to obtain the CO_2 saturated solution prior to electrolysis. The CO_2 was continuously purged within a linked working electrode chamber that was employed for the product analysis and stability tests. A cationic exchange membrane (CMI-7000S) was employed as a separator between the working electrode and counter electrode chamber in the cell. The working electrode and reference electrode (Ag/AgCl) were in the same compartment, whereas the counter electrode was in a separate compartment. The generated gas was transferred into the gas chromatography (GC, Shimadzu GC-2014, Column: Silica gel, thermal conductive detector (TCD), the column temperature was raised from 40 to 250 °C at a heating rate of 3 °C min^{-1}; the injector temperature was set at 70 °C, with a heating velocity of 25 °C min^{-1}; the sampling volume of 50 μL was taken by a gas-tight syringe (Hamilton™, 50 μL) in order to analyze the gas products.

3. Results and discussion

In order to form the nanoporous structure, a polycrystalline Au electrode was electrochemically alloyed and dealloyed in a mixture of ethylene glycol and 1.5 M $ZnCl_2$ using cyclic voltammetry. Scheme 1 presents a schematic diagram, illustrating the formation of the NP Au-Zn and the further acid treatment of the NP Au-Zn electrode. Fig. 1A depicts a lower magnification SEM image of the formed NP Au-Zn, showing that interconnected networks were homogeneously formed on the Au surface. The pore sizes of the formed NP Au-Zn were from ~250–500 nm in diameter as seen in the higher magnification SEM image (Fig. 1B). The formed NP Au-Zn was further treated with H_2SO_4 followed by a mild calcination at 150 °C for 1 h, resulting in the formation of larger sized nanopores with diameters ranging from ~750 to 1000 nm, as shown in the SEM images (Fig. 1C and D). Fig. 2A presents the EDX spectra of the Au, NP Au-Zn, and NP Au electrodes. Two weak Zn peaks were observed in the NP Au-Zn, which confirmed that a small amount of Zn still remained during the electrochemical alloying/dealloying fabrication process. However, the incorporated Zn was removed by the acid treatment. The crystalline phase of the three different Au electrodes were determined via XRD, as displayed in Fig. 2B. The typical face-centered-cubic (fcc) Au diffraction peaks, including (111), (200), (220), (311), and (222) planes (JCPDS no. 01-1172) [27] were observed for all of the Au electrodes. The additional peaks labelled by asterisks were derived from the formed Au/Zn alloy [28]. It is worth noting that all the Au/Zn alloy diffraction peaks disappeared following the acid treatment, indicating that the incorporated Zn was removed from the NP Au-Zn. This was further confirmed via the X-ray photoelectron spectroscopic (XPS) survey scans. A noticeable Zn $2p_{3/2}$ peak appeared at 1022.58 eV in the NP Au-Zn (Fig. S1 A), but disappeared after the acid treatment (Fig. S2B). Further quantitative analysis revealed that the amount of Zn in the NP Au-Zn was ~7.0%. The high-

resolution Zn $2p_{3/2}$ XPS spectrum is displayed in Fig. 3A, revealing that its binding energy was slightly higher than that of pure Zn (1022.00 eV) [29]. Fig. 3B and C present the high-resolution Au 4f XPS spectra of the NP Au, prior to and following the acid treatment, respectively. The Au $4f_{7/2}$ and $4f_{5/2}$ peaks for the untreated NP Au-Zn were observed at 84.19 and 87.86 eV, which shifted toward a lower binding energy of 0.01 and 0.02 eV of the NP Au ($4f_{7/2}$, 84.18 eV, and $4f_{5/2}$, 87.84 eV), respectively. This further confirmed the formation of the Au/Zn alloy in the NP Au-Zn and the removal of Zn, subsequent to the acid treatment of the NP Au-Zn, which was consistent with the EDX and XRD results.

The EASA of the Au, NP Au-Zn, and NP Au was estimated by the simultaneous formation and reduction of gold oxide. Fig. 4 depicts the corresponding CVs of the three Au electrodes, showing that the NP Au-Zn possessed the highest current density. The formation of gold oxide started at ~1.10 V; one notable anodic peak was observed for the polycrystalline Au electrode; whereas two anodic peaks appeared for the nanoporous Au electrodes, indicating that the surface structure was changed during the alloying/dealloying process [30]. The reduction charge was calculated by integrating the area of the reduction peak centered at ~0.9 V vs. Ag/AgCl [31]. As listed in Table S1, the smooth Au electrode had a RF of 1.05; and the formed NP Au possessed the highest EASA (2.54 cm^2), which was over 79 times higher than its geometric surface area. However, following the acid treatment, the EASA was decreased to 1.59 cm^2; thus the RF was decreased from 79.37 to 49.68, which was consistent with the SEM images displayed in Fig. 1. After the acid treatment, the pore size was significantly increased due to the dissolution of the Zn species incorporated during the electrochemical alloying/dealloying process.

To study the electrocatalytic activity of the synthesized Au electrodes, LSV were recorded from 0.0 to -0.8 V (vs. RHE) in a CO_2-saturated 0.1 M $NaHCO_3$ (pH 6.65) solution. Fig. 5A compares the LSV curves of the Au, NP Au-Zn, and NP Au electrodes recorded at 20 mV s^{-1}. The current density was dramatically increased from the Au to the treated NP Au-Zn electrode. For instance, at -0.8 V, the cathodic current of the formed NP Au was 42.79 mA cm^{-2}, which was 26 times higher than that of the Au (1.62 mA cm^{-2}), and three times higher than that of the NP Au-Zn (14.26 mA cm^{-2}). The current densities of the NP Au-Zn and NP Au electrodes were also calculated based on their EASAs (Fig. S2), further showing that the NP Au had superior catalytic activity toward the CO_2 reduction. EIS was employed to measure the charge-transfer resistance for the electrochemical reduction of CO_2 on the prepared different Au electrodes. Fig. 5B displays the Nyquist plots of the Au, NP Au-Zn, and NP Au electrodes recorded in a CO_2-saturated 0.1 M $NaHCO_3$ solution at −0.4 V (vs. RHE), where Z_{re} and Z_{im} expressed the real and imaginary components, respectively. The impedance curves of the Au and NP Au-Zn electrodes revealed two semicircles in the full range of frequency, whereas the formed NP Au
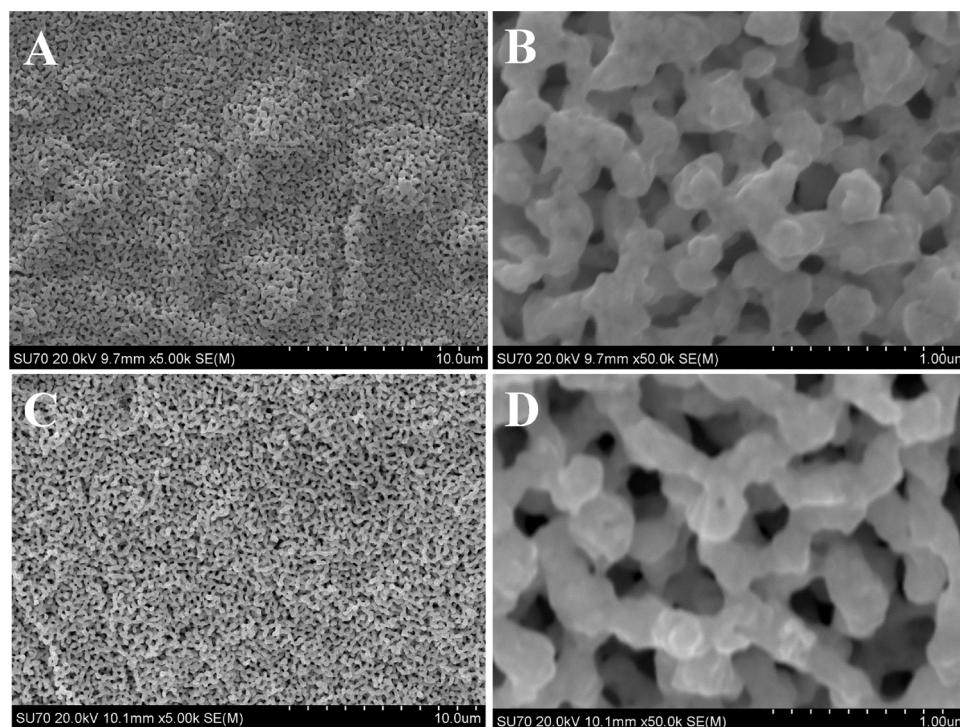
Fig. 1. Low-magnification SEM images of (A) the NP Au-Zn electrode, and (B) the acid-treated NP Au electrode; High-magnification SEM images of (C) the NP Au-Zn electrode and (D) the acid-treated NP Au electrode.
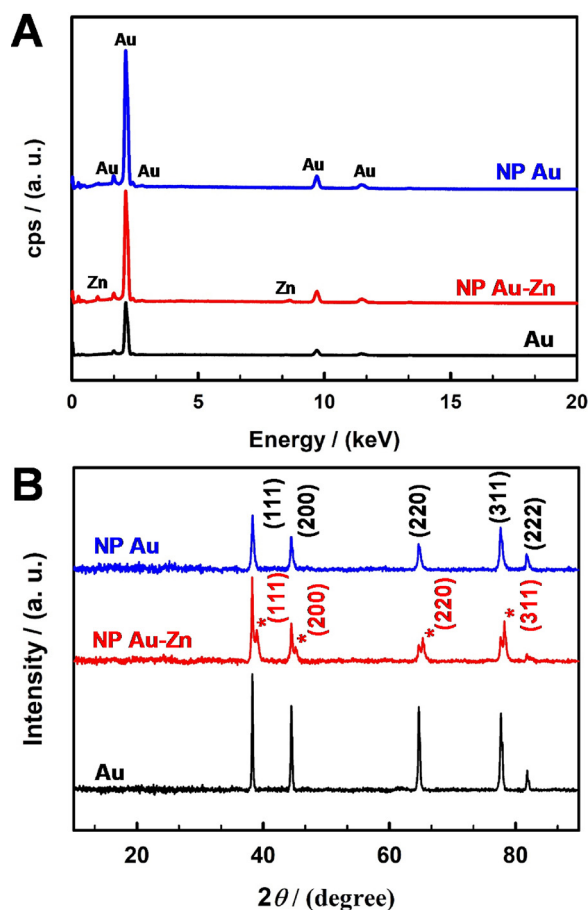
Fig. 2. (A) EDX spectra of the three different Au electrodes and (B) XRD patterns of the three different Au electrodes.

exhibited a semi-circle and a half semi-circle. The two semi-circles corresponded to the two charge transfer resistances (R1 and R2) [32,33] that appeared in the equivalent electrical circuit (insert, Fig. 5B), which was employed to fit the EIS spectra. The corresponding fitted results for each element, along with the percentage of errors, are listed in Table S2. All of the fitting element errors were less than 5%, indicating that the proposed equivalent electrical circuit effectively fitted the impedance data. It was noted that the NP Au electrode possessed a much lower charge-transfer resistance for both R1 and R2 than did the other Au electrodes. Moreover, a short Warburg impedance (Ws) associated with R2, and two constant phase elements (CPE1 and CPE2) were included in the equivalent circuit to fit the impedance spectra effectively. This indicated that all of the Au electrodes exhibited some capacitor-like behavior, and that a diffusion resistance was also involved during the electrochemical reduction of CO_2. To investigate the kinetics of the CO_2 reduction, Tafel plots of the Au, NP Au-Zn and NP Au electrodes were measured by LSV in a CO_2-saturated 0.1 M $NaHCO_3$ electrolyte, yielding a slope of 126, 88 and 57 mV dec^{-1} for the smooth Au, NP Au-Zn and NP Au electrodes, respectively (Fig. 6). The much lower Tafel slope of the NP Au electrode indicated a much faster first-electron transfer of the CO_2 reduction to CO compared to the polycrystalline Au and NP Au-Zn electrodes [1,14].

To determine the Faradic efficiency (FE) and to assess the stability of the NP Au-Zn and the NP Au electrodes, CA was performed in a CO_2-saturated 0.1 M $NaHCO_3$ solution for 10 h, where CO_2 was continuously purged into the solution during the entire procedure. Fig. 7A and 7B present the CA curves of the NP Au-Zn and formed NP Au electrodes under applied potentials of −0.4, −0.5, and −0.6 V, respectively. For comparison, the CA curves of the smooth Au electrode are presented in Fig. S3. The current density was increased with the increase of the applied cathodic potential for all the electrodes, where the steady-state curves were obtained during the entire electrolysis, indicating the high stability of the electrodes. The current densities of the NP Au (Fig. 7B) were much higher than that of the polycrystalline Au (Fig. S3) and the NP Au-Zn (Fig. 7A), further confirming that the acid treatment significantly enhanced the electrocatalytic activity of the NP Au for CO_2
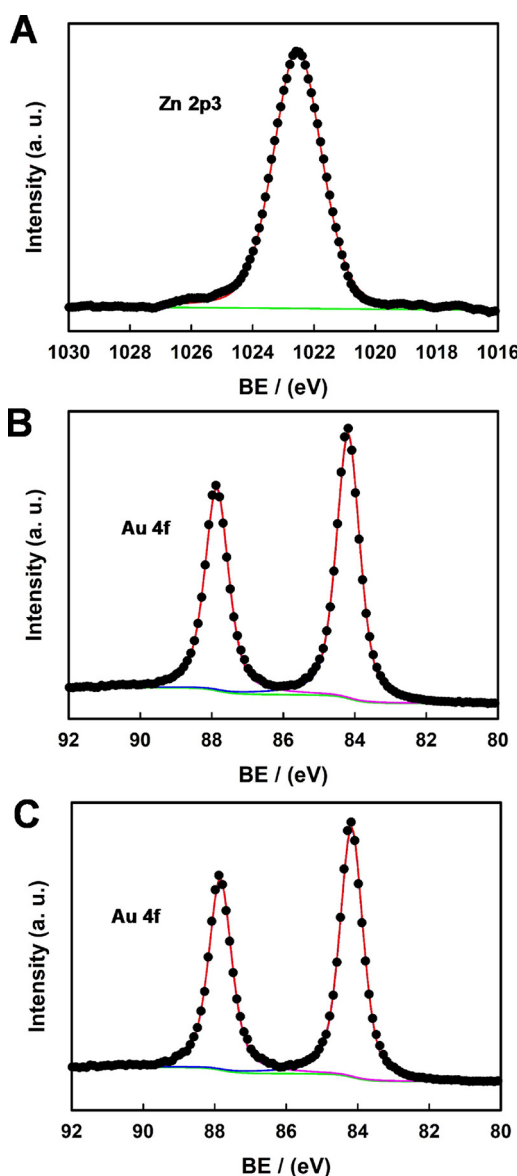
Fig. 3. High-resolution XPS spectra of the Zn $2p_{3/2}$ region of the formed NP Au-Zn (A), the Au 4f region of the NP Au-Zn, (B) the treated NP Au (C) electrodes.
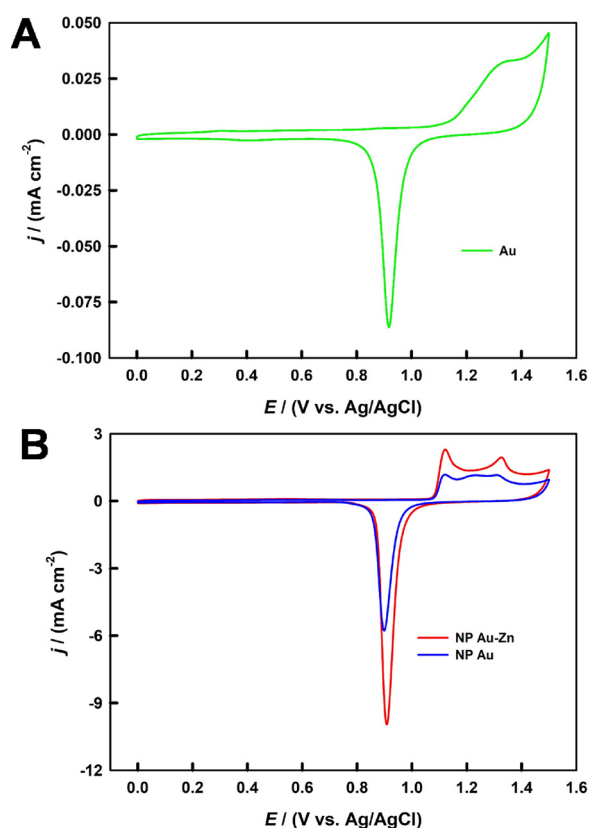

Fig. 4. Cyclic voltammograms of: (A) the smooth polycrystalline Au electrode; and (B) the NP Au-Zn electrode (red) and the acid treated NP Au electrode (blue). Scan rate: 20 mV s^{-1}; Electrolyte: 0.1 M H$_2$SO$_4$(For interpretation of the references to colour in this figure legend, the reader is referred to the web version of this article).

reduction. Our GC analysis revealed that CO was produced as the primary gas product under all applied potentials during the electrochemical reduction of CO$_2$ on both the NP Au-Zn and NP Au, whereas H$_2$ was the dominant product on the polycrystalline Au. Fig. 8A and B compare the FE and CO production rate of the polycrystalline Au, the NP Au-Zn and the NP Au electrodes, respectively; and their corresponding values are summarized in Table S3, showing that the polycrystalline Au favoured the hydrogen evolution reaction with less than 45% FE for CO formation due to the limited active sites available at a smooth Au surface for the CO$_2$ reduction. In contrast, a superb affinity for the selective CO generation from the CO$_2$ reduction was attained with ~90% FE at the NP Au-Zn and ~95% FE at the NP Au electrodes, revealing that the formation of nanoporous structure adequately suppressed the hydrogen evolution reaction. This is consistent with the observations reported in the literature, where the FE for CO formation was improved when the morphology of the Au catalyst was changed from a smooth surface to a nanostructured electrode [14,19,20]. As the CO formation rate at the smooth Au electrode was so low, it was enlarged by 10 times in Fig. 8B for comparison. The CO generation was increased with the increase of the cathodic potential from −0.4 to

−0.6 V for all the Au electrodes. The rates of the CO formation on the NP Au-Zn and the NP Au electrodes were substantially higher than that at the smooth Au electrode, for instance, 49.8 times greater at the NP Au-Zn electrode and 151.8 times higher at the NP Au electrode at the applied potential of −0.6 V (Table S3). This was further evidenced by a video clip (Fig. S4) that was recorded during the electrochemical reduction of CO$_2$ in a CO$_2$-saturated 0.1 M NaHCO$_3$ solution at −0.6 V, where the CO evolution was much faster on the NP Au in contrast to the NP Au-Zn electrode. Such a significant increase in the catalytic activity after the acid treatment might be attributed to a few factors, including (i) the removal of Zn, (ii) the change of EASA, (iii) the increase of the pore size, and (iv) the creation of new active sites.

Firstly, to investigate the impact of Zn, we prepared two nanoporous electrodes, Au and Au-Zn, with almost the same EASA. The NP Au-Zn electrode was fabricated by employing 10 cycles of the electrochemical alloying/dealloying of a polycrystalline Au. The EASA of the formed NP Au-Zn was 2.05 cm^2. For comparison, a Zn-free NP Au with an EASA of 2.02 cm^2 was fabricated by the electrochemical alloying/dealloying for 40 cycles followed by the H$_2$SO$_4$ acid treatment. Fig. S5 displays the current densities of the NP Au-Zn and the Zn-free NP Au electrodes normalized by their EASAs, revealing that the presence of Zn decreased the catalytic activity of the NP Au electrode. Secondly, as seen in Table S1, the formed NP Au electrode possessed a smaller EASA compared with the NP Au-Zn electrode; however, it exhibited greater FE and approximately three times higher CO generation rate than the NP Au-Zn electrode at all the tested cathodic potentials as shown in Fig. 8A and B, indicating that the enhanced catalytic activity was not due to the change of the EASA. Thirdly, to study the pore size effect, we prepared four Zn-free NP Au by varying the number of electrochemical alloying/dealloying cycles from 10 to 40 and followed by the H$_2$SO$_4$ acid
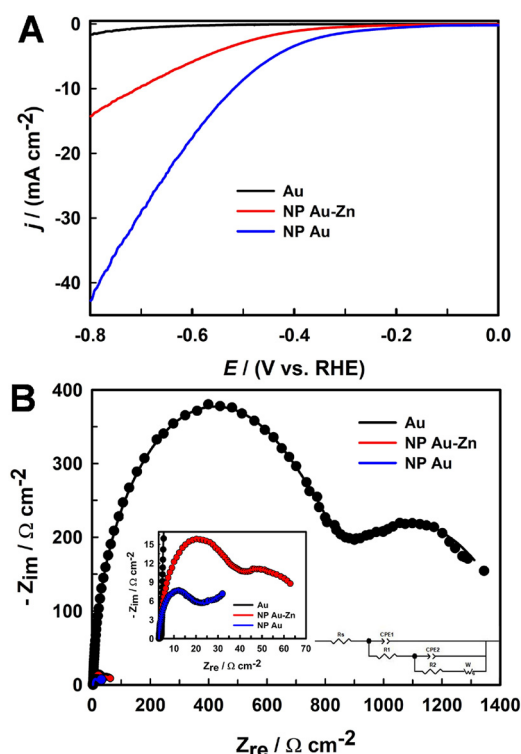
Fig. 5. (A) LSVs of the three different Au electrodes recorded in a CO_2-saturated 0.1 M solution. (B) The corresponding Nyquist plots measured at -0.4 V. Inset: the equivalent electric circuit used for fitting the EIS data, where Rs = solution resistance; R1 and R2 = charge-transfer resistances; CPE1 and CPE2 = constant phase elements; Ws = Warburg impedance (short).
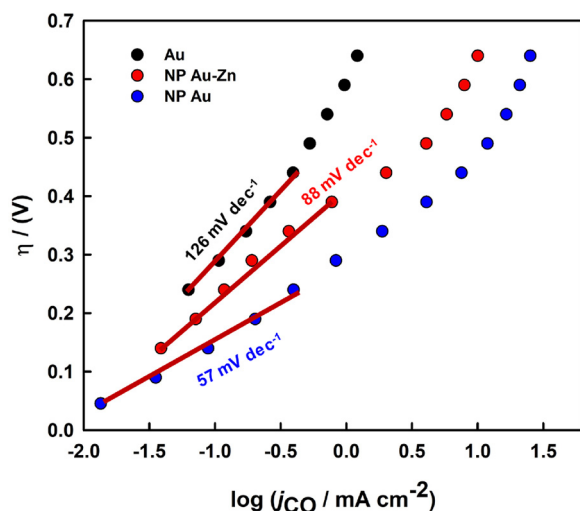

Fig. 6. Tafel plots for the electrochemical reduction of CO_2 at the Au, NP Au-Zn and NP Au electrodes.

treatment. Fig. S6 presents the SEM images of the fabricated Zn-free NP Au electrodes, showing that the pore size was increased with the increase of the number of the alloying/dealloying cycles. This was further confirmed by the electrochemical measurements, showing that the EASA was increased from 1.14 to 2.02 cm^2 and that the RF was raised from 35.64 to 63.09 (Table S1) with the increase of the number of alloying/dealloying cycles from 10 to 40. As seen in Fig. S7 A, the current density of the prepared Zn-free different NP Au electrodes, based upon the geometrical surface area, was increased with the increase of the alloying/dealloying cycles due to the increase of the EASA. However, when the current was normalized by the EASA (Fig. S7B), the current
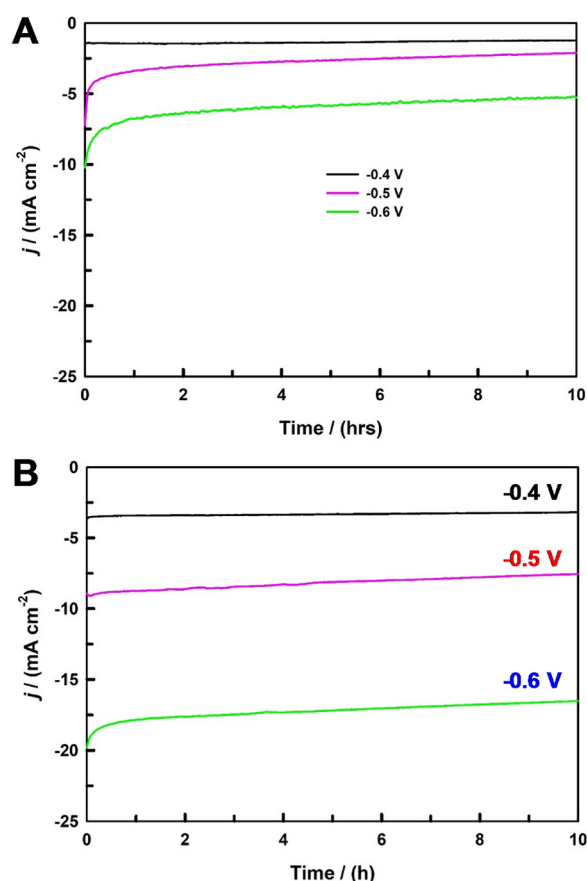

Fig. 7. The CA curves of the NP Au-Zn electrode (A) and the acid treated NP Au electrode (B), recorded under different applied electrode potentials in CO_2 saturated 0.1 M NaHCO$_3$ over the 10 h electrolysis.

density was slightly increased with the increase of the number of the alloying/dealloying cycles from 10 to 30; but it was marginally decreased when it was increased to 40 alloying/dealloying cycles, indicating that the pore size did not play a critical role in the enhancement of the catalytic activity of the formed NP Au. Finally, to explore whether new active sites were created during the removal of Zn using the acid treatment, we carried out the Pb UPD analysis of the polycrystalline Au, NP Au-Zn and NP Au electrodes in a 0.1 M KClO$_4$ containing 50 μM Pb(NO$_3$)$_2$ solution. As seen in Fig. S8, a dominated stripping peak appeared at 0.047 V (vs. Ag/AgCl) at the NP Au-Zn electrode, which corresponded to the Pb stripping from the Au(111) surface [20,34]; whereas the strong stripping peak was shifted to 0.30 V at the NP Au electrode, which was associated with the Pb stripping from the Au(110) surface, revealing that new active sites were created during the acid treatment. All the aforementioned suggested that the removal of Zn and the creation of new active sites, facilitated by the acid treatment, played the key roles in the significant enhancement of the catalytic activity of the NP Au-Zn electrode for the efficient CO_2 reduction.

4. Conclusions

In summary, we demonstrated a facile electrochemical alloying/ dealloying approach in conjunction with an acid treatment to fabricate a unique 3D nanoporous Au network structure with a large EASA, which served as a high-performance electrocatalyst for the efficient and selective conversion of CO_2 to CO. The formed NP Au showed a superb FE of 95.86% with an extremely high CO production rate at the applied potential of -0.6 V vs. RHE in a CO_2-saturated 0.1 M NaHCO$_3$ solution. The creation of new active sites during the removal of the Zn from the
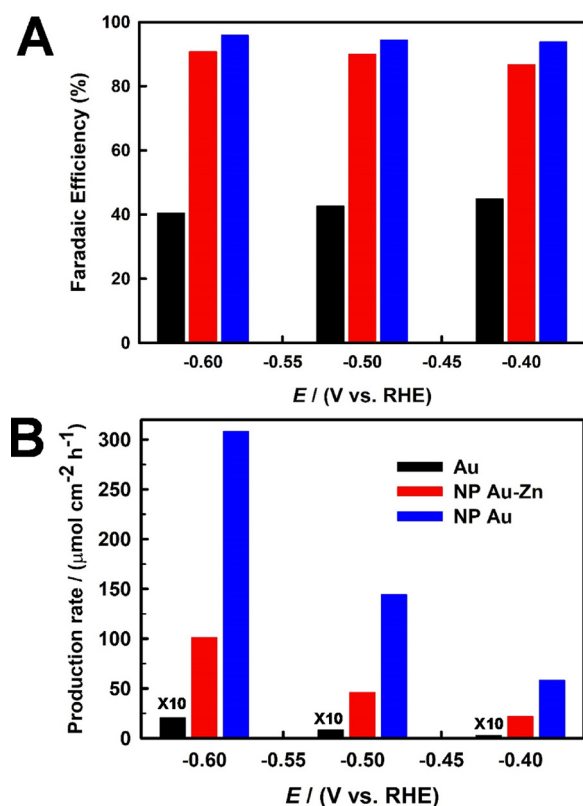
Fig. 8. (A) FE of the CO formation on the polycrystalline Au (black bar), the NP Au-Zn (red bar) and the acid-treated NP Au electrodes (blue bar); (B) the CO production rates during the electrolysis of CO_2 under different applied potentials on the Au, the NP Au-Zn and the acid-treated NP Au electrodes (For interpretation of the references to colour in this figure legend, the reader is referred to the web version of this article).

NP Au-Zn played a vital role in the increase of the catalytic activity. The high current density, low charge-transfer resistance, large production rate, and high stability makes the unique NP Au electrode developed in this study promising for the efficient electrochemical reduction of CO_2. Moreover, this study might inspire researchers to ponder the significant effects of the active sites and the surface structure of the Au in order to design desirable electrocatalysts for robust CO_2 reduction.

Conflict of interest

The authors declare no competing financial interest.

Acknowledgements

Appendix A. Supplementary data

References

[1] M. Liu, Y. Pang, B. Zhang, P.D. Luna, O. Voznyy, J. Xu, X. Zheng, C.T. Dinh, F. Fan, C. Cao, F.P.G. de Arquer, T.S. Safaei, A. Mepham, A. Klinkova, E. Kumacheva, T. Filleter, D. Sinton, S.O. Kelley, E.H. Sargent, Nature 537 (2016) 382–386.

[2] N.V. Rees, R.G. Compton, Energy Environ. Sci. 4 (2011) 403–408.

[3] Y.S. Ham, S. Choe, M.J. Kim, T. Lim, S.-K. Kim, J.J. Kim, Appl. Catal. B: Environ. 208 (2017) 35–43.

[4] J.-H. Kim, H. Woo, S.-W. Yun, H.-W. Jung, S. Back, Y. Jung, Y.-T. Kim, Appl. Catal. B: Environ. 213 (2017) 211–215.

[5] M.N. Hossain, J. Wen, A. Chen, Sci. Rep. 7 (2017) 3184.

[6] W. Li, B. Herkt, M. Seredych, T.J. Bandosz, Appl. Catal. B: Environ. 207 (2017) 195–206.

[7] M.N. Hossain, J. Wen, S.K. Konda, M. Govindhan, A. Chen, Electrochem. Commun. 82 (2017) 16–20.

[8] N. Gutierrez-Guerra, L. Moreno-Lopez, J.C. Serrano-Ruiz, J.L. Valverde, A. de Lucas-Consuegr, Appl. Catal. B: Environ. 188 (2016) 272–282.

[9] S. Gao, Y. Lin, X. Jiao, Y. Sun, Q. Luo, W. Zhang, D. Li, J. Yang, Y. Xie, Nature 529 (2016) 68–71.

[10] M. Aresta, A. Dibenedetto, A. Angelini, Chem. Rev. 114 (2014) 1709–1742.

[11] H.A. Hansen, J.B. Varley, A.A. Peterson, J.K. Nørskov, J. Phys. Chem. Lett. 4 (2013) 388–392.

[12] D. Kim, J. Resasco, Y. Yu, A.M. Asiri, P. Yang, Nat. Commun. 5 (2014) 4948.

[13] Q. Lu, J. Rosen, Y. Zhou, G.S. Hutchings, Y.C. Kimmel, J.G. Chen, F. Jiao, Nat. Commun. 5 (2014) 3242.

[14] Y.H. Chen, C.W. Li, M.W. Kanan, J. Am. Chem. Soc. 134 (2012) 19969–19972.

[15] H. Mistry, R. Reske, Z. Zeng, Z.-J. Zhao, J. Greeley, P. Strasser, B.R. Cuenya, J. Am. Chem. Soc. 136 (2014) 16473–16476.

[16] E.B. Nursanto, H.S. Jeon, C. Kim, M.S. Jee, J.H. Koh, Y.J. Hwang, B.K. Min, Catal. Today 260 (2016) 107–111.

[17] G.A. Olah, G.K.S. Prakash, A. Goeppert, J. Am. Chem. Soc. 133 (2011) 12881–12898.

[18] W. Zhu, Y.-J. Zhang, H. Zhang, H. Lv, Q. Li, R. Michalsky, A.A. Peterson, S. Sun, J. Am. Chem. Soc. 136 (2014) 16132–16135.

[19] G.B. Stevens, T. Reda, B. Raguse, J. Electroanal. Chemistry 526 (2002) 125–133.

[20] A.S. Hall, Y. Yoon, A. Wuttig, Y. Surendranath, J. Am. Chem. Soc. 137 (2015) 14834–14837.

[21] R. Kortlever, I. Peters, C. Balemans, R. Kas, Y. Kwon, G. Mul, M.T.M. Koper, Chem. Commun. 52 (2016) 10229–10232.

[22] D.R. Kauffman, D. Alfonso, C. Matranga, H. Qian, R. Jin, J. Am. Chem. Soc. 134 (2012) 10237–10243.

[23] T. Cheng, Y. Huang, H. Xiao, W.A. Goddard III, J. Phys. Chem. Lett. 8 (2017) 3317–3320.

[24] S. Back, M.S. Yeom, Y. Jung, ACS Catal. 5 (2015) 5089–5096.

[25] A.A. Peterson, J.K. Nørskov, J. Phys. Chem. Lett. 3 (2012) 251–258.

[26] Y. Pang, T. Burdyny, C.-T. Dinh, M.G. Kibria, J.Z. Fan, M. Liu, E.H. Sargent, D. Sinton, Green Chem. 19 (2017) 4023–4030.

[27] H.J. Wang, C.W. Zou, B. Yang, H.B. Lu, C.X. Tian, H.J. Yang, M. Li, C.S. Liu, D.J. Fu, J.R. Liu, Electrochem. Commun. 11 (2009) 2019–2022.

[28] R.E. Cable, R.E. Schaak, Chem. Mater. 19 (2007) 4098–4104.

[29] J.-H. Lin, Y.-J. Huang, Y.-P. Su, C.-A. Liu, R.S. Devan, C.-H. Ho, Y.-P. Wang, H.-W. Lee, C.-M. Chang, Y. Liou, Y.-R. Ma, RSC Adv. 2 (2012) 2123–2127.

[30] X.J. Chen, Y.Y. Wang, J.J. Zhou, W. Yan Li, H.X.J.J. Zhu, Anal. Chem. 80 (2008) 2133–2140.

[31] Z. Liu, A. Nemec-Bakk, N. Khaper, A. Chen, Anal. Chem. 89 (2017) 8036–8043.

[32] D.-W. Yang, Q.-Y. Li, F.-X. Shen, Q. Wang, L. Li, N. Song, Y.-N. Dai, J. Shi, Electrochim. Acta 189 (2016) 32–37.

[33] V. Lates, A. Falch, A. Jordaan, R. Peach, R.J. Kriek, Electrochim. Acta 128 (2014) 75–84.

[34] A. Hamelin, J. Lipkowski, J. Electroanal. Chem. 171 (1984) 317–330.